PNAS RESEARCH ARTICLE | EARTH, ATMOSPHERIC, AND PLANETARY SCIENCES

Elevated atmospheric CO_2 drove an increase in tropical cyclone intensity during the early Toarcian hyperthermal

Qing Yan[a,b,1], Xiang Li[c,1], David B. Kemp[d], Jiaqi Guo[c], Zhongshi Zhang[e], and Yongyun Hu[c,2]

Edited by Kerry Emanuel, Massachusetts Institute of Technology, New Harbor, ME; received January 18, 2023; accepted May 11, 2023

The occurrence of sedimentary storm deposits around the Tethys Ocean during the early Toarcian hyperthermal (~183 Ma) suggests that intensified tropical cyclone (TC) activity occurred in response to CO_2 rise and marked warming. However, this hypothesized linkage between extreme warmth and storm activity remains untested, and the spatial pattern of any changes in TCs is unclear. Here, model results show that there were two potential storm genesis centers over Tethys during the early Toarcian hyperthermal located around the northwestern and southeastern Tethys. The empirically determined doubling of CO_2 concentration that accompanied the early Toarcian hyperthermal (~500 to ~1,000 ppmv) leads to increased probability of stronger storms over Tethys, in tandem with more favorable conditions for coastal erosion. These results match well with the geological occurrence of storm deposits during the early Toarcian hyperthermal and confirm that increased TC intensity would have accompanied global warming.

tropical cyclone | paleoclimate modeling | early Toarcian hyperthermal

Present-day anthropogenic carbon fluxes and associated warming are widely predicted to lead to significant changes in extreme weather over the coming decades (1), with significant socioeconomic consequences. In particular, climate models predict that the proportion of category 4 to 5 tropical cyclones (TCs) and average peak TC wind speeds will increase as a direct consequence of elevated CO_2 and warmer sea surface temperatures (1, 2). Empirical evidence to support these projections is relatively sparse, although an increase in the frequency of intense TCs and mean intensity have been directly observed over the past ~40 y (1, 3–5). Over longer timescales, however, the links between CO_2, temperature, and TC activity are less clear (6–10).

Past extreme warming events in Earth history (known as "hyperthermals") offer an opportunity to assess the mechanistic links between extreme climate change and storm behavior, as well as the timescales over which such changes can occur. In particular, the early Toarcian hyperthermal (also known as the Toarcian oceanic anoxic event or Jenkyns Event, ~183 Ma) offers a potentially useful analogue for understanding the responses of the Earth's weather systems to large-scale carbon release. This event has been linked to the large-scale emission of carbon from volcanism and/or surficial reservoirs such as methane hydrates and permafrost (11–13). Tropical sea surface temperatures increased significantly in response to these emissions (14, 15), and there were associated changes in atmospheric CO_2, ocean redox, and global chemical weathering (16–19). The Toarcian hyperthermal may have lasted for ~1 million y (e.g., ref. 13), with the carbon emissions associated with the event driving an approximate doubling of CO_2 (~500 to 1,000 ppmv) over perhaps a few tens of thousands to hundreds of thousands of years (16, 17, 19) (Fig. 1). An emerging feature of the early Toarcian hyperthermal is an increase in the abundance of sedimentary storm deposits coeval with the event (20–22), prompting the suggestion that carbon release and global warming at this time directly triggered an increase in the abundance and/or frequency of intense TCs (21) (Fig. 1, see also *Methods*). Nevertheless, this hypothesis has not yet been robustly tested, and the precise relationship between CO_2 change, warming, and storminess is unclear. Similarly, the spatial pattern of changes in storm activity at the early Toarcian hyperthermal is uncertain, owing to the relative paucity of sites where early Toarcian storm deposits have been recorded (e.g., Fig. 1).

To address these issues, we have used a coupled global climate model to test the hypothesis that increased atmospheric CO_2 in the early Toarcian triggered an intensification of TCs. We quantify changes in TC potential intensity and spatial distribution of genesis potential in response to the inferred changes in atmospheric CO_2 at this time and determine the major controls on these changes. Our results provide a deep-time perspective on how Earth's weather systems respond to large-scale carbon release and warming.

Significance

Past extreme warming events in Earth's history offer a unique opportunity to assess the links between global warming and storm behavior. We present global climate modeling results that confirm the hypothesized linkage between extreme warmth from CO_2 rise and intensified storm activity based on geological evidence during the early Toarcian hyperthermal (~183 mya) and identify the underpinning dynamic mechanisms. Our results provide strong geological support for the idea that storm intensity will increase in the future due to global warming and provide a deep-time perspective on how Earth's weather systems respond to large-scale carbon release.

Author affiliations: [a]Nansen-Zhu International Research Centre, Institute of Atmospheric Physics, Chinese Academy of Sciences, Beijing 100029, China; [b]Key Laboratory of Meteorological Disaster/Collaborative Innovation Center on Forecast and Evaluation of Meteorological Disasters, Nanjing University of Information Science and Technology, Nanjing 210044, China; [c]Laboratory for Climate and Ocean-Atmosphere Studies, Department of Atmospheric and Oceanic Sciences, School of Physics, Peking University, Beijing 100871, China; [d]State Key Laboratory of Biogeology and Environmental Geology and Hubei Key Laboratory of Critical Zone Evolution, School of Earth Sciences, China University of Geosciences, Wuhan 430074 China; and [e]Department of Atmospheric Science, School of Environmental Studies, China University of Geosciences, Wuhan 430074, China

Author contributions: D.B.K., Z.Z., and Y.H. designed research; X.L. and J.G. performed research; Q.Y. analyzed data; and Q.Y. and D.B.K. wrote the paper.

The authors declare no competing interest.

This article is a PNAS Direct Submission.

[1]Q.Y. and X.L. contributed equally to this work.

[2]To whom correspondence may be addressed. Email: yyhu@pku.edu.cn.

This article contains supporting information online at https://www.pnas.org/lookup/suppl/doi:10.1073/pnas.2301018120/-/DCSupplemental.

Published July 10, 2023.

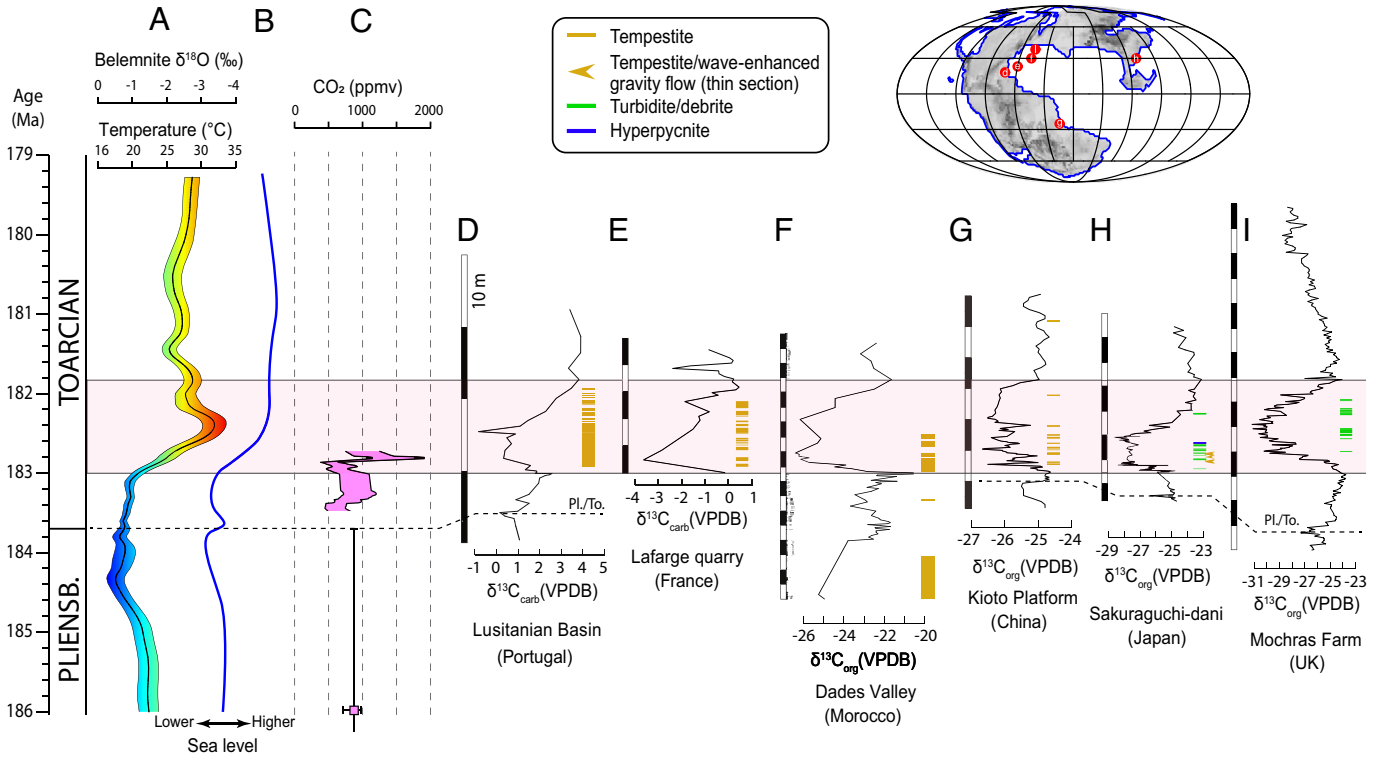

Fig. 1. Paleoclimate change and selected storm deposits across the early Toarcian hyperthermal. (*A*) Oxygen isotope ($\delta^{18}O$) composition of belemnites (13) that is smoothed with a 10% LOESS function and with 2σ CI based on bootstrapping. Seawater temperatures derived from these data assume a $\delta^{18}O$ of seawater of ~0‰ (15). (*B*) Relative sea-level change (13). (*C*) Atmospheric CO_2 concentration based on fossil leaf stomatal density (16, 23). (*D–I*) Carbon isotope ($\delta^{13}C$) and sedimentology data for Lusitanian Basin, Portugal (21) (*D*), Lafarge quarry, France (21) (*E*), Dades Valley, Morocco (21) (*F*), Kioto Platform, China (22) (*G*), Sakuraguchi-dani, Japan (24) (*H*), and Mochras Farm, United Kingdom (25) (*I*). The early Toarcian hyperthermal in each section is demarcated by the carbon-isotope excursion (i.e., light red shading). Age scale for the carbon-isotope excursion is from ref. 19. Note the typical restriction of tempestites, turbidites, and hyperpycnites to the carbon-isotope excursion interval in each section. The approximate locations of sedimentary storm deposits are shown in the upper right map (gray shading indicates land). Pl./To. = Pliensbachian–Toarcian boundary. Further details are provided in the *Methods* section.

Results and Discussion

Enhanced Storm Activity during the Early Toarcian Hyperthermal. During the early Toarcian hyperthermal, large-scale environmental conditions support two TC genesis potential centers across Tethys in our simulations. One is concentrated on northwestern Tethys; the other is distributed in the southeastern part (Fig. 2*A*). Storm generation over the two centers is relatively more active during July–October (defined as the storm season) in the Northern Hemisphere and during January–April in the Southern Hemisphere (Fig. 2*B*), which is similar to modern conditions (26). The regions favorable for TC production are generally within the areas bounded by the 26.5 °C isotherm and high potential intensity (>70 m/s) during the storm season (Fig. 2*A*). In addition, large-scale steering flow that controls the general pattern of storm trajectory (27, 28) shows an anticyclonic circulation over northern Tethys during the storm season (Fig. 2*A*), with an obvious easterly flow at low latitudes (~5 to 20°N). This favors a storm forming over northwestern Tethys to make landfall along the continental coasts of northern Gondwana. A westward steering flow is observed within the ~15 to 30°S band over southern Tethys (Fig. 2*A*), conducive to TC landfalls over the southwestern tropical Tethyan margin. Importantly, the modeled locations of active storm activity over Tethys during the early Toarcian hyperthermal are supported by geological occurrences of storm deposits at this time (Fig. 2*A*).

The enhanced storm activity during the early Toarcian hyperthermal was previously argued to be linked with the CO_2 rise and warming (20–22). To test this hypothesis, we set up a pair of sensitivity experiments and examine how TC may vary with the empirically determined approximate doubling of CO_2 (560 to 1,120 ppmv) during the early Toarcian hyperthermal, as determined from fossil plant stomatal density change (16) and fossil leaf-wax carbon-isotope composition (17) (see also *Methods*). Our results demonstrate that TC potential intensity is enhanced over almost the entire Tethys Ocean during the storm season in response to higher CO_2 concentration, accompanied by a uniform ocean warming (Fig. 3*A*). In particular, there is an increased possibility for stronger storms over Tethys during the early Toarcian hyperthermal, manifested by a shift in the tail of the probability distribution toward extremely high potential intensity (e.g., >75 m/s; Fig. 3 *B* and *C*). This rightward shift in the probability distribution is more profound over northern Tethys, around which the majority of sedimentary storm deposits during the early Toarcian hyperthermal have been found (Fig. 2*A*).

Atmospheric CO_2 concentrations during the early Toarcian hyperthermal may have exceeded 2,000 ppmv based on maximum likely values from fossil leaf stomatal density (16), so we further test the variation of potential intensity using a more extreme warming scenario (CO_2 = 2,800 ppmv). The results also point to a significant shift to extremely strong storms under such a high (but still geologically plausible) CO_2 scenario, and the higher the CO_2 concentration, the more extreme the storms (Fig. 3 *B* and *C*). This is supported by the findings based on modern continental configurations (29).

Spatial Pattern of Change in Storm Activity. Despite an overall warming and higher potential intensity, there are obvious spatial differences in the variation of TC genesis potential across Tethys in

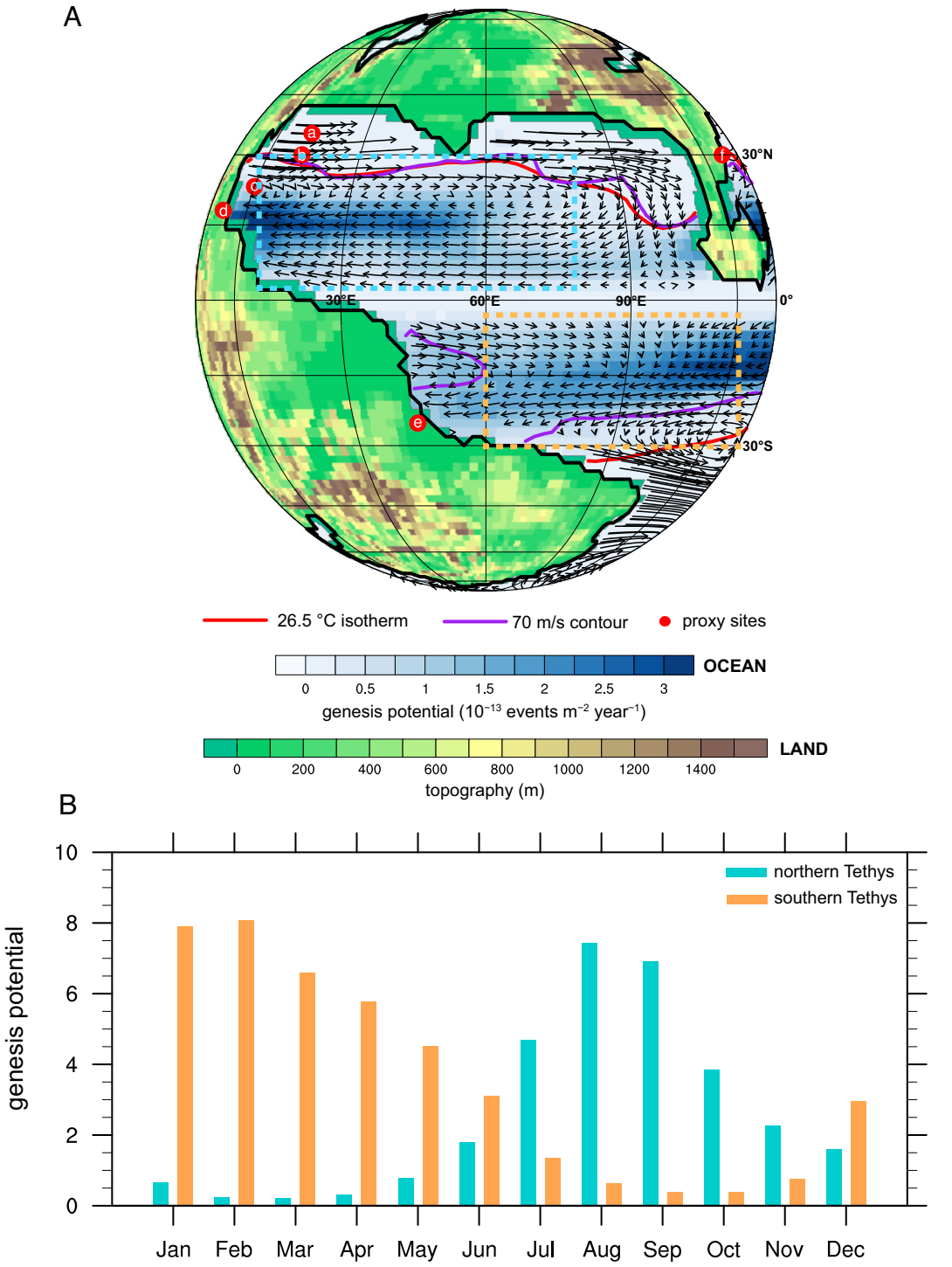

Fig. 2. Spatial pattern and seasonal cycle of tropical cyclone genesis potential over Tethys during the early Toarcian hyperthermal. (*A*) Geographic distribution of annual mean genesis potential (blue shadings). The red lines show the 26.5 °C isotherm. The purple lines show the 70 m s^{-1} contour for potential intensity. The red dots show the locations of sedimentary storm deposits (tempestites) previously recorded during the early Toarcian hyperthermal (a: Dotternhausen, Germany (21); b: Lafarge quarry, France (20), c: Lusitanian Basin, Portugal (21), d: Dades Valley, Morocco (21), e: Kioto Platform, China (22), f: Sakuraguchi-dani, Japan (24). (*B*) Seasonal cycle in monthly genesis potential (units: no./month) averaged over northern (5 to 30°N; 0 to 80°E) and southern (5 to 30°S; 60 to 140°E) Tethys. The approximate domain of the defined northern and southern Tethys is shown in *A* as dashed cyan and orange rectangles, respectively.

response to higher CO_2 (Fig. 4). Genesis potential shows a general increase over northern Tethys during the storm season, with more profound change at the western part. This suggests a westward shift and increased favorability for storm generation. In contrast, there is a quasi-eastward shift in genesis potential over southern Tethys, with more favorable conditions for storm formation in the eastern part. Moreover, under a higher CO_2 scenario, an anticyclonic anomaly in steering flow appears over northwestern Tethys, with anomalous northward/northeastward flows around the continental coasts. This implies that coastal regions of northern Gondwana might be more susceptible to storm strikes and hence increased coastal erosion. Over the tropics of southern Tethys, there is an anomalous eastward flow at the low latitudes (~5 to 20°S) but a westward flow at the relatively higher latitudes, suggesting less

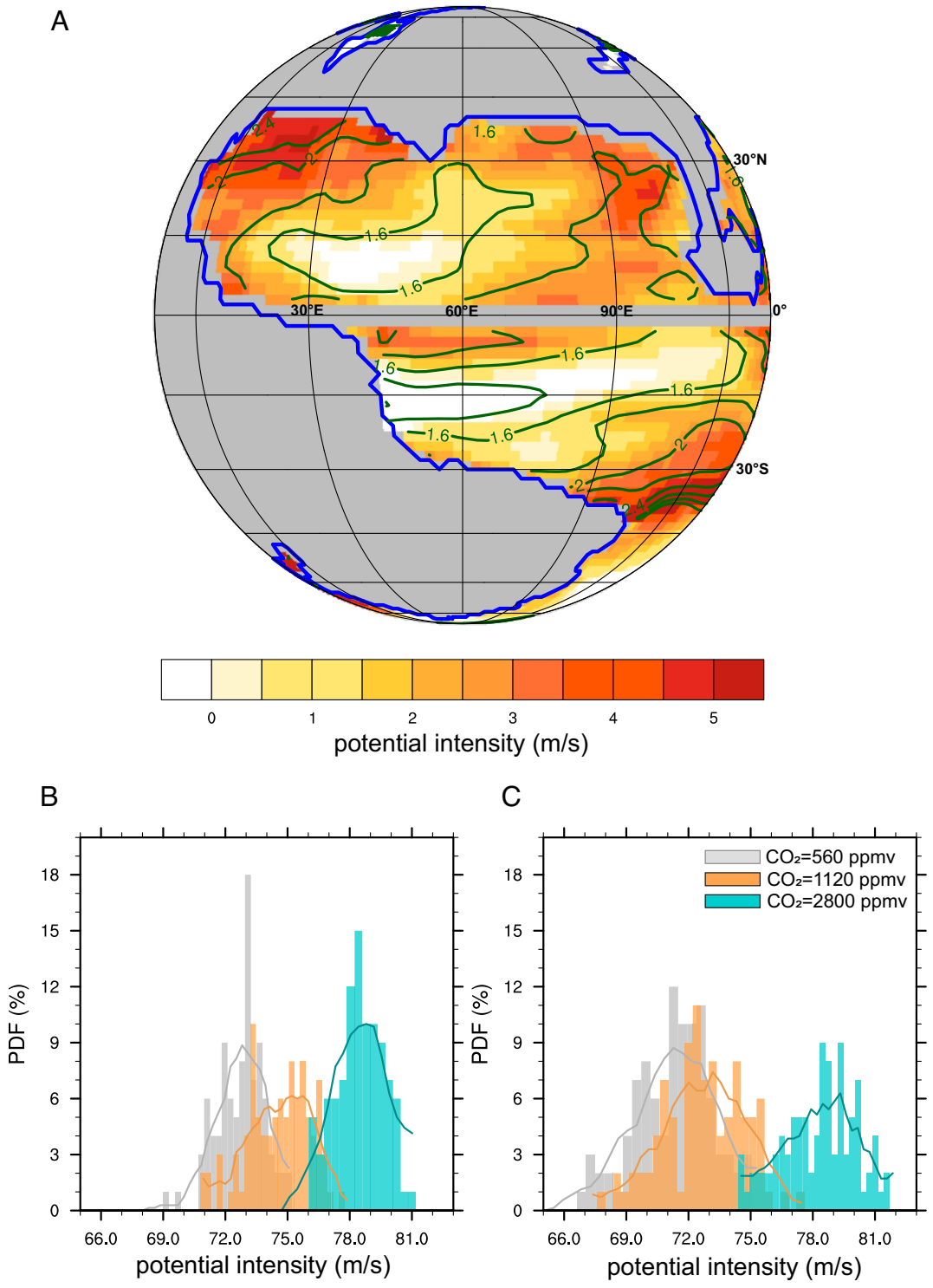

Fig. 3. Change in potential intensity and its probability distribution during the storm season in response to higher CO_2 concentration during the early Toarcian hyperthermal. (*A*) The differences in potential intensity (shading; m/s) and sea surface temperature (contours; °C) between higher (1,120 ppmv) and lower (560 ppmv) CO_2 concentrations during the early Toarcian hyperthermal. The thick blue lines represent the outline of early Toarcian continents. (*B* and *C*) Probability distribution function (PDF) of potential intensity with the 560 ppmv (gray), 1,120 ppmv (orange), and 2,800 ppmv (cyan) CO_2 concentrations over northern (b; 5 to 30°N, 0 to 80°E) and southern (c; 5 to 30°S, 60 to 140°E) Tethys. The thick lines are the smoothed probability density distribution. Storm season is defined as Jul–Oct in the northern hemisphere and as Jan–Apr in the southern hemisphere.

favorable conditions for TC landfalls at low latitudes but more favorable conditions for landfalls at middle latitudes.

In addition to the inferred TC activity over Tethys, increases in genesis potential and mean potential intensity are observed over almost the entire tropical ocean in response to increased CO_2 concentration during the early Toarcian hyperthermal (*SI Appendix*, Fig. S1). In particular, there is an increased possibility for more intense storms across the tropical ocean, including Panthalassa, based on the estimated probability distribution (*SI Appendix*, Fig. S2). This is supported by evidence for storm deposits on the margin of western Panthalassa during the early Toarcian hyperthermal (24).

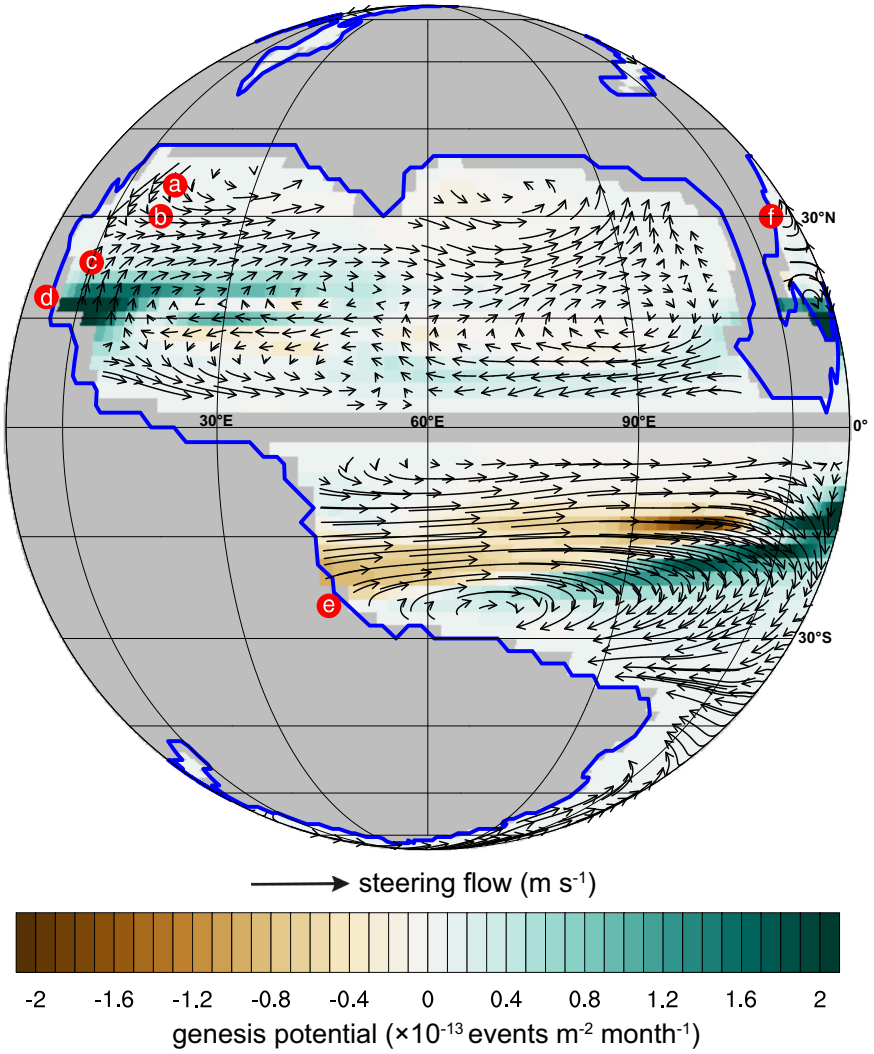

Fig. 4. Changes in genesis potential (shadings) and large-scale steering flow (vectors; m/s) during the storm season in response to higher CO_2 concentration during the early Toarcian hyperthermal. The units of genesis potential are events m^{-2} $month^{-1}$($\times 10^{-13}$). The differences are computed between the experiments with higher (1,120 ppmv) and lower (5,60 ppmv) CO_2 concentrations. The red dots show the locations of sedimentary storm deposits (tempestites) during the early Toarcian hyperthermal (20–22, 24) (see Fig. 2 for details). The thick blue lines represent the outline of early Toarcian continents. Storm season is defined as Jul-Oct in the northern hemisphere and as Jan-Apr in the southern hemisphere.

Mechanisms behind the Change in Storm Activity. The shift in TC genesis potential during the early Toarcian hyperthermal is tied to the changes in large-scale environmental factors that arise from the adjustment of regional temperature structure and the associated variations of atmospheric circulations. In response to increased CO_2 concentration, the entire Tethys Ocean experiences higher potential intensity, but with relatively larger changes in the northwestern and southeastern parts (Figs. 3*A* and 5 *A* and *E*). This is largely attributable to the intensified thermodynamic disequilibrium over the two regions that results mainly from the reduced surface wind speed, with positive contributions from larger thermodynamic efficiency (Fig. 5 *B* and *F* and *SI Appendix*, Fig. S3). Furthermore, the uneven warming in the atmosphere leads to a zonal dipole pattern in meridional temperature gradient in northern Tethys, which results in enhanced (reduced) westerly to the east (west) of ~40°E based on thermal wind balance and hence gives rise to larger (smaller) vertical wind shear (Fig. 5*C* and *SI Appendix*, Fig. S4). Similarly, the meridional temperature gradient in southern Tethys exhibits an increase at the western part and a decrease to the east, which closely matches the pattern of vertical wind shear anomaly (Fig. 5*G*). The anomaly of moisture entropy deficit is characterized by negative and positive values in the western and eastern part of northern Tethys, respectively (Fig. 5*D*). The reduced moist entropy deficit over northern Tethys is dominated by increased midtropospheric relative humidity, whereas the decreased temperature contrast between the midtroposphere and the surface that weakens the strength of the surface heat fluxes largely contributes to the enhanced moist entropy deficit (Fig. 5*D* and *SI Appendix*, Fig. S5). In southern Tethys, the smaller moist entropy deficit in the eastern part is largely caused by increased midtropospheric relative humidity, while the larger moist entropy deficit in the western part is dominated by the dampened temperature contrast (Fig. 5*H*). Overall, the zonal shift of genesis potential is linked with the variations of potential intensity, vertical wind shear, and moist entropy deficit (Fig. 5), but the relative contributions of individual environmental factors vary across Tethys (*SI Appendix*, Fig. S6).

Implications and Conclusions. Through a set of coupled climate model experiments, our results suggest that the doubling of CO_2 concentrations that likely characterized the early Toarcian hyperthermal led to increased favorability for stronger TCs to

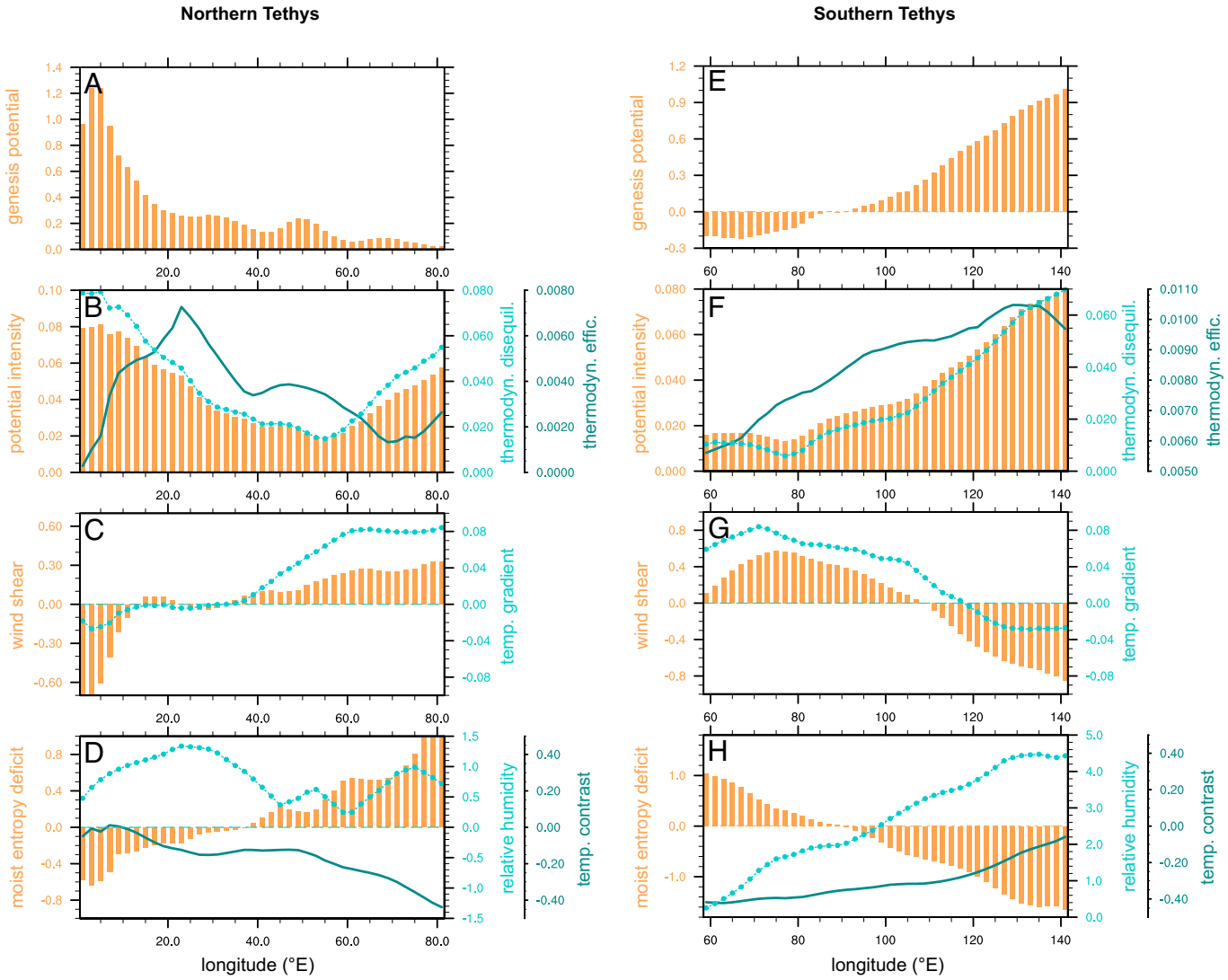

Fig. 5. Differences in zonal mean genesis potential and environmental variables during storm season in response to higher CO_2 concentration during the early Toarcian hyperthermal. Over northern Tethys (0 to 80°E): (*A*) Genesis potential. (*B*) Potential intensity [2log(PI); bars; m/s], thermodynamic disequilibrium [$log\,(h_0^* - h)$; dotted line; m/s], and thermodynamic efficiency [$log\left(\frac{SST - T_o}{T_o}\right)$; thick line; m/s]. (*C*) Vertical wind shear between 200 and 850 hPa (bars; m/s) and absolute meridional temperature gradient (dotted line; $\times 10^{-6}$ °C/m) in the troposphere. (*D*) Moist entropy deficit (bars; $\times 10^{-2}$), relative humidity (dotted line; %) at 600 hPa, and vertical temperature contrast (thick line; °C) between surface and midtroposphere (600 hPa). (*E–H*) same as (*A–D*) but for southern Tethys (60 to 140°E).

develop over the northwestern/southeastern Tethys, as well as other ocean regions at tropical paleolatitudes. Our results confirm the hypothesized linkage between extreme warmth from CO_2 rise and intensified storm activity during the early Toarcian hyperthermal.

In addition to the early Toarcian hyperthermal, increased storm intensity associated with global warming has also been observed in other warmer-than-present time intervals in Earth history. For example, there is growing evidence for increased tempestite deposition (30–32) during the Paleocene Eocene Thermal Maximum (~55 Ma)—an event characterized by a global temperature rise of ~5 to 8 °C (33). An increase in global TC intensity has also been predicted for the Pliocene warm period (~5 to 3 Ma) (34, 35) when the planet warmed by ~3 °C with increased atmospheric CO_2 based on ref. 36. Extremely strong storms were documented over the North Atlantic (37–39) during the peaking warming of the Last Interglacial (~129 to 124 ka) in which global sea surface temperature was ~1 °C higher than present (40) owing to changes in Earth's orbital configuration and hence insolation. Warmer sea surface temperatures also contributed to the recorded intense hurricanes over the North Atlantic during several intervals of the last two millennia (9). This geological evidence emphasizes the general expectation that increases in TC intensity accompany global warming. Interestingly, observations point to increased mean TC intensity and higher frequency of category 4 to 5 TCs under current warming (1, 3–5), though with differences across ocean basins. Thus, we should expect more intense TCs in a future warmer climate, which is consistent with the majority of future projections (1, 2).

There are a number of limitations in our work and findings to be considered. The model predicts significantly higher SSTs during the early Toarcian hyperthermal in response to higher CO_2 concentration (*SI Appendix*, Fig. S7), but the magnitude of warming may be underestimated compared to the limited proxy-based estimates that exist (14, 15). This may be partially attributable to the lower climate sensitivity of the climate model used here (41) or limitations with the reliability of proxy temperature estimates based on the chemistry of extinct fauna (i.e., belemnites) (14). However, this discrepancy has limited influence on the qualitative results reported here, as the Earth still experiences much stronger storms in our

extreme warming scenario (CO_2 = 2,800 ppmv; Fig. 3 *B* and *C*) in which the modeled warming matches better with the proxy data (*SI Appendix*, Fig. S7). Additionally, potential intensity and genesis potential used here have been proven useful to depict the intensity and location of actual TCs on regional scales, but they provide no information on the behaviors of individual storms (e.g., storm tracks). This hampers the direct comparison of our results with the known storm-related sedimentary deposits. On the other hand, sedimentary storm deposits do not have the stratigraphic and temporal resolution needed to resolve spatial patterns of TC intensity, which in turn is insufficient to constrain the model results. Thus, combinations of high-resolution (e.g., 25-km resolution) climate model or other downscaling techniques (e.g., ref. 42) and additional proxies for TCs would be useful to further assess the linkage between extreme warmth and storm activity in the future. Nevertheless, our results and the available geological evidence now clearly point to increased storm intensity associated with global warming, which is what we observe in current warming. The evidence we present from the early Toarcian hyperthermal aligns with the emerging evidence from other past warm periods that experienced a marked increase in intense storms, which is also fully consistent with future projections determined by modeling (1, 2). Ultimately, therefore, this study highlights the value in studying how past warming events can be used to inform predictions of future extreme climate change.

Methods

Sedimentary Storm Deposits. Sedimentary indicators of storm events have been recorded during the early Toarcian hyperthermal from a number of localities worldwide (Fig. 1). In the western Tethys region, tempestites have been recorded in the Central High Atlas Basin (Dades Valley) of Morocco (21), the Lusitanian Basin of Portugal (21, 43), France (20, 44), and Germany (21, 45). Further east in Tethys, siliciclastic tempestites are recorded in carbonate-dominated successions at Nianduo and Wolong (Kioto Platform), Tibet (22). In Panthalassa, putative tempestites were observed in thin section from a marginal marine succession at Sakuraguchi-dani, Japan (24). Importantly, tempestites in all these locations are nearly always restricted to the early Toarcian hyperthermal (i.e., the carbon isotope excursion) where peak temperatures and maximum atmospheric pCO_2 occurred (Fig. 1). Sequence stratigraphic work has indicated that significant eustatic sea-level rise accompanied the early Toarcian hyperthermal (46), with this rise likely driven by thermal expansion of seawater and polar ice melting (13). As such, the sudden occurrence of storm deposits restricted to the early Toarcian hyperthermal cannot be attributed to a drop in sea level and consequent deposition of strata above storm wave base. On the contrary, rising sea level across the early Toarcian hyperthermal emphasizes that storm events likely increased in magnitude in order to impinge on the sea floor (21). In other locations, sedimentary deposits indicative of high-energy conditions and/or increased sediment fluxes (such as turbidites and hyperpycnites) have been recorded (Fig. 1). Locations include Japan (Sakuraguchi-dani) (24), the United Kingdom (Mochras Farm borehole and Yorkshire) (21, 25), the North Sea (Dutch Central Graben) (47), and Portugal (48). Although not strictly diagnostic of storm activity, these deposits are generally restricted to the early Toarcian hyperthermal and are suggestive of higher-energy conditions and/or increased sediment loading despite increased sea level.

Climate Model. The Community Earth System Model (CESM) version 1.2.2 (49) is a fully coupled global climate model developed by the National Center for Atmospheric Research. The model consists of components for the atmosphere, ocean, land, sea ice, and rivers, and geophysical fluxes across these components are exchanged via a central coupler. The resolution of the atmospheric component, Community Atmosphere Model version 4 (CAM4), is 3.75° in longitude by 3.75° in latitude, with 26 vertical levels. The land component, Community Land Model version 4 (CLM4), has the same horizontal resolution as CAM4. Here, the prognostic carbon–nitrogen model with dynamic vegetation is turned on to simulate unmanaged vegetation including tree, grass, and shrub plant functional types. The river transport model directs all runoff to oceans and is run with the default resolution (0.5° × 0.5°). The ocean component, Parallel Ocean Program version 2 (POP2), has a nominal 3° irregular horizontal grid (116 and 100 grid points in the meridional and zonal directions, respectively), with 60 vertical levels. The sea ice component (i.e., Community Sea Ice Model version 4) is run on the same horizontal grid as POP2. The CESM model has been validated for modern climates and has also been successfully implemented in a variety of paleoclimate studies spanning from the Precambrian (~540 Ma) (50, 51) to mid-Holocene (~6 ka) (52). Equally, CESM has relatively better performance in depicting the key features of past climates (53, 54). Thus, we used the fully coupled CESM version 1.2.2 to provide state-of-the-art computer simulations of past climate states.

Experimental Design. The paleogeographic map for the early Toarcian (*SI Appendix*, Fig. S8) is from the paleo-digital elevation model (paleoDEM) of ref. 55, which is a digital representation of paleotopography and paleobathymetry reconstructed back in time. The paleoDEM describes distributions of deep oceans, shallow seas, lowlands, and mountainous regions, and it is an estimate of the elevation of the land surface and depth of the ocean basins. Some modifications are made for the Tethys following refs. 21 and 56, and we do not consider the isolated small islands due to the coarse resolution used here. No ice sheets are prescribed in the simulations. The paleogeography is produced at an original resolution of 1° × 1°, from which we generated model-resolution land–sea mask, topography, and bathymetry.

To investigate the sensitivity of TC activity to atmospheric CO_2 concentrations, three simulations are performed with 2×, 4×, and 10× the preindustrial concentration (280 ppmv). Estimates of early Toarcian hyperthermal CO_2 concentrations and changes are inherently uncertain given the limitations of the available proxies (e.g., ref. 17 and references therein). However, the 2× preindustrial concentration (560 ppmv) is close to the pre-early Toarcian hyperthermal estimate of atmospheric CO_2 determined by both fossil leaf stomatal density data (16) and fossil leaf wax carbon-isotope data (17) (~500 to 700 ppmv). The 4× preindustrial concentration (1,120 ppmv) is close to the estimated peak CO_2 concentration of the early Toarcian hyperthermal based on fossil leaf wax carbon-isotope data (17) (~1,000 ppmv) and close to the minimum concentration estimated by fossil leaf stomatal density data (16) (~1,250 ppmv). The 10× preindustrial concentration (2,800 ppmv) exceeds the maximum estimated peak CO_2 concentration of the early Toarcian hyperthermal based on fossil leaf wax carbon-isotope data (17) (~1,200 ppmv) but is closer to the maximum estimated concentration based specifically on fossil Ginkgoales stomatal density data (16) (~2,300 ppmv). The solar constant is set to 1341.4 W m^{-2} for the early Toarcian, considering that solar radiation increases linearly at an approximate rate of 0.08% per 10 Myr (57) to the present-day value of 1360.89 W m^{-2}. Orbital parameters in the simulations are set the same as the present-day values.

Following the guidelines of the Deep-Time Model Intercomparison Project (58), the simulations are integrated for ≥2,000 model y to reach equilibrium states at which the net radiation at the top of the atmosphere averaged over the last 100 model y is less than 0.1 W m^{-2} (*SI Appendix*, Table S1). Monthly outputs from the last 100 model y in each experiment are archived and used for the relevant statistical analysis (i.e., the calculation of potential intensity and genesis potential).

Potential Intensity. Potential intensity is the theoretical maximum intensity of a storm constrained by the thermodynamic state of the atmosphere and sea surface (59, 60). It has been proven useful to measure the climatology and variability of actual storm intensity (61–63). Potential intensity is defined as

$$PI = \sqrt{\frac{C_k}{C_d}\frac{SST - T_o}{T_o}(h_0^* - h)}, \qquad [1]$$

where C_k and C_d are the enthalpy and momentum surface exchange coefficients, respectively, T_o is the mean outflow temperature, h_0^* is the enthalpy of air saturated at the sea surface temperature and pressure, and h is the enthalpy of an ambient boundary layer parcel. The term $\frac{SST - T_o}{T_o}$ depicts the thermodynamic efficiency, and the term $(h_0^* - h)$ measures thermodynamic disequilibrium (61). We estimate the contributions from the two factors by squaring and taking the natural logarithm of Eq. **1**:

$$2\log(PI) = \log\left(\frac{SST - T_o}{T_o}\right) + \log\left(h_0^* - h\right) + \log\frac{C_k}{C_d}, \qquad [2]$$

Genesis Potential Index. We employ a Genesis Potential Index (GPI) that summarizes large-scale environmental factors that are important to TC formation to predict the regions where storms may generate. GPI has high skills in predicting the spatial pattern of actual TC genesis (26, 63, 64) (e.g., *SI Appendix*, Fig. S9) and shows similar performance compared with downscaling method (65, 66), and hence are widely employed to study TC activity in past, present, and future climates (67–70). The GPI used here is defined as

$$GPI = \frac{a[min(|\eta|, 4\times10^{-5})]^3[max(PI-35,0)]^2}{\chi^{4/3}(25+VS)^4}, \quad [3]$$

where a is a normalizing coefficient, PI is the potential intensity, VS is the vertical wind shear, χ is the moist entropy deficit, and η is the low-level absolute vorticity. Briefly, vertical wind shear is defined as the magnitude of the vector difference between the 200 and 850 hPa horizontal winds, as the most profound difference in TC environmental wind profiles generally appears between these two levels (71), and the vertical wind shear measured between 200 and 850 hPa generally has the strongest negative correlation with storm intensity (72). Vertical wind shear generally weakens storm formation and development via shearing the convective towers and ventilating the storm's core with subsaturated air (73). Moist entropy deficit is adopted to assess the midtropospheric moisture content (at 600 hPa) and is determined by the ratio of the difference in moist entropy that moist convection must eliminate to the strength of the surface fluxes supplying the moisture (65–67):

$$\chi = \frac{s^* - s_m}{s_0^* - s^*}, \quad [4]$$

where s_0^* and s^* are the saturation moist entropies of the sea surface and free troposphere (600 hPa), respectively, and s_m represents the moist entropy of the middle troposphere (600 hPa). Larger moist entropy deficit suggests less favorable conditions for TC generation and vice versa. Low-level absolute vorticity is computed at 850 hPa and acts as a spin-up mechanism by inducing important synoptic convergence that favors cyclone formation (74). Overall, regions of high genesis potential identify the areas in which TC genesis is possible; low values are found only in regions that cannot support the deep convection that defines such systems. More information concerning individual genesis factors and GPI is given in ref. 69.

Data, Materials, and Software Availability. The estimated genesis potential data and relevant climatic variables based on CESM simulations are available at https://zenodo.org/record/7972338 (75). More CESM simulation results are available from the corresponding author Prof. Yongyun Hu, yyhu@pku.edu.cn. The CESM code can be downloaded from the official website: https://www.cesm.ucar.edu/models/. The code for calculating potential intensity is provided by Prof. Kerry Emanuel and is available at https://texmex.mit.edu/pub/emanuel/TCMAX/.

ACKNOWLEDGMENTS. We thank the Editor and the two anonymous reviewers for their extremely helpful comments, which greatly helped to improve the quality of the original manuscript. This study was funded by the National Natural Science Foundation of China (41888101 and 42022036) and the Youth Innovation Promotion Association by Chinese Academy of Sciences (2019080). Simulations are conducted at the High-performance Computing Platform of Peking University. D.B.K. acknowledged the support of the International Geoscience Program 739.

1. S. I. Seneviratne *et al.*, "Weather and climate extreme events in a changing climate. In climate change 2021: The physical science basis" in *Contribution of Working Group I to the Sixth Assessment Report of the Intergovernmental Panel on Climate Change*, V. Masson-Delmotte *et al.*, Eds. (Cambridge University Press, 2021), pp. 1513–1766.
2. T. Knutson *et al.*, Tropical cyclones and climate change assessment: Part II: Projected response to anthropogenic warming. *Bull. Am. Meteorol. Soc.* **101**, E303–E322 (2020).
3. N. Kang, J. B. Elsner, Trade-off between intensity and frequency of global tropical cyclones. *Nat. Clim. Change* **5**, 661–664 (2015).
4. J. P. Kossin, K. R. Knapp, T. L. Olander, C. S. Velden, Global increase in major tropical cyclone exceedance probability over the past four decades. *Proc. Natl. Acad. Sci. U.S.A.* **117**, 11975–11980 (2020).
5. T. Knutson *et al.*, Tropical cyclones and climate change assessment: Part I: Detection and attribution. *Bull. Am. Meteorol. Soc.* **100**, 1987–2007 (2019).
6. J. P. Donnelly, J. D. Woodruff, Intense hurricane activity over the past 5,000 years controlled by El Niño and the West African monsoon. *Nature* **447**, 465–468 (2007).
7. M. E. Mann, J. D. Woodruff, J. P. Donnelly, Z. Zhang, Atlantic hurricanes and climate over the past 1,500 years. *Nature* **460**, 880–883 (2009).
8. J. Haig, J. Nott, G. Reichart, Australian tropical cyclone activity lower than at any time over the past 550–1,500 years. *Nature* **505**, 667–671 (2014).
9. J. P. Donnelly *et al.*, Climate forcing of unprecedented intense-hurricane activity in the last 2000 years. *Earth's Future* **3**, 49–65 (2015).
10. E. J. Wallace, S. Coats, K. A. Emanuel, J. P. Donnelly, Centennial-scale shifts in storm frequency captured in paleohurricane records from the Bahamas arise predominantly from random variability. *Geophys. Res. Lett.* **48**, e2020GL091145 (2021).
11. S. P. Hesselbo *et al.*, Massive dissociation of gas hydrate during a Jurassic oceanic anoxic event. *Nature* **406**, 392–395 (2000).
12. D. B. Kemp, A. L. Coe, A. S. Cohen, L. Schwark, Astronomical pacing of methane release in the Early Jurassic period. *Nature* **437**, 396–399 (2005).
13. W. Ruebsam, B. Mayer, L. Schwark, Cryosphere carbon dynamics control early Toarcian global warming and sea level evolution. *Glob. Planet. Change* **172**, 440–453 (2019).
14. T. R. Bailey, Y. Rosenthal, J. M. McArthur, B. van de Schootbrugge, M. F. Thirlwall, Paleoceanographic changes of the Late Pliensbachian-Early Toarcian interval: A possible link to the genesis of an oceanic anoxic event. *Earth Planet. Sci. Lett.* **212**, 307–320 (2003).
15. W. Ruebsam, M. Reolid, N. Sabatino, D. Maseti, L. Schwark, Molecular paleothermometry of the early Toarcian climate perturbation. *Glob. Planet. Change* **195**, 103351 (2020).
16. J. C. McElwain, J. Wade-Murphy, S. P. Hesselbo, Changes in carbon dioxide during an oceanic anoxic event linked to intrusion into Gondwana coals. *Nature* **435**, 479–482 (2005).
17. W. Ruebsam, M. Reolid, L. Schwark, $\delta^{13}C$ of terrestrial vegetation records Toarcian CO_2 and climate gradients. *Sci. Rep.* **10**, 117 (2020).
18. D. B. Kemp, G. Suan, A. Fantasia, S. Jin, W. Chen, Global organic carbon burial during the Toarcian oceanic anoxic event: Patterns and controls. *Earth Sci. Rev.* **231**, 104086 (2022).
19. D. B. Kemp, D. Selby, K. Izumi, Direct coupling between carbon release and weathering during the Toarcian oceanic anoxic event. *Geology* **48**, 976–980 (2020).
20. G. Suan *et al.*, Palaeoenvironmental significance of Toarcian black shales and event deposits from southern Beaujolais. France. *Geol. Mag.* **150**, 728–742 (2013).
21. F. N. Krencker *et al.*, Toarcian extreme warmth led to tropical cyclone intensification. *Earth Planet. Sci. Lett.* **425**, 120–130 (2015).
22. Z. Han, X. Hu, D. B. Kemp, J. Li, Carbonate-platform response to the Toarcian Oceanic Anoxic Event in the southern hemisphere: Implications for climatic change and biotic platform demise. *Earth Planet. Sci. Lett.* **489**, 59–71 (2018).
23. M. Steinthorsdottir, V. Vajda, Early Jurassic (late Pliensbachian) CO_2 concentrations based on stomatal analysis of fossil conifer leaves from eastern Australia. *Gondwana Res.* **27**, 932–939 (2015).
24. K. Izumi, D. B. Kemp, S. Itamiya, M. Inui, Sedimentary evidence for enhanced hydrological cycling in response to rapid carbon release during the early Toarcian oceanic anoxic event. *Earth Planet. Sci. Lett.* **481**, 162–170 (2018).
25. W. Xu *et al.*, Evolution of the Toarcian (Early Jurassic) carbon-cycle and global climatic controls on local sedimentary processes (Cardigan Bay Basin, UK). *Earth Planet. Sci. Lett.* **484**, 396–411 (2018).
26. S. J. Camargo, A. H. Sobel, A. G. Barnston, K. A. Emanuel, Tropical cyclone genesis potential index in climate models. *Tellus A* **59**, 428–443 (2007).
27. A. J. Colbert, B. J. Soden, Climatological variations in North Atlantic tropical cyclone tracks. *J. Clim.* **25**, 657–673 (2012).
28. C. H. Ho, J. J. Baik, J. H. Kim, D. Y. Gong, C. H. Sui, Interdecadal changes in summertime typhoon tracks. *J. Clim.* **17**, 1767–1776 (2004).
29. R. L. Korty, K. A. Emanuel, M. Huber, R. A. Zamora, Tropical cyclones downscaled from simulations with very high carbon dioxide levels. *J. Clim.* **30**, 649–667 (2017).
30. J. Zamagni, M. Mutti, P. Ballato, A. Kosir, The paleocene-eocene thermal maximum (PETM) in shallow-marine successions of the Adriatic carbonate platform (SW Slovenia). *Geol. Soc. Am. Bull.* **124**, 1071–1086 (2012).
31. V. Pujalte, A. Robador, A. Payros, J. M. Samso, Input of coarse-grained siliciclastics into the Pyrenean Basin during the PETM (2): A river-dominated fan delta within a carbonate platform system. *Rend. Online Soc. Geo. It.* **31**, 179–180 (2014).
32. A. N. Al-Fattah, A. I. Al-Juboury, I. M. Ghafor, Paleocene-eocene thermal maximum record of northern iraq: Multidisciplinary indicators and an environmental scenario. *Jordan J. Earth Environ. Sci.* **11**, 126–145 (2020).
33. F. A. McInerney, S. L. Wing, The paleocene-eocene thermal maximum: A perturbation of carbon cycle, climate and biosphere with implications for the future. *Annu. Rev. Earth Planet. Sci.* **39**, 489–516 (2011).
34. Q. Yan *et al.*, Enhanced intensity of global tropical cyclones during the mid-Pliocene warm period. *Proc. Natl. Acad. Sci. U.S.A.* **113**, 12963–12967 (2016).
35. A. V. Fedorov, C. M. Brierley, K. A. Emanuel, Tropical cyclones and permanent El Niño in the early Pliocene epoch. *Nature* **463**, 1066–1070 (2010).
36. A. M. Haywood *et al.*, The pliocene model intercomparison project phase 2: Large-scale climate features and climate sensitivity. *Clim. Past* **16**, 2095–2123 (2020).
37. P. J. Hearty, A. C. Neumann, D. S. Kaufman, Chevron ridges and runup deposits in the Bahamas from storms late in oxygen-isotope substage 5e. *Quat. Res.* **50**, 309–322 (1998).
38. P. J. Hearty, B. R. Tormey, Sea-level change and superstorms; geologic evidence from the last interglacial (MIS 5e) in the Bahamas and Bermuda offers ominous prospects for a warming Earth. *Mar. Geol.* **390**, 347–365 (2017).
39. Q. Yan, R. L. Korty, T. Wei, N. Jiang, A westward shift in tropical cyclone potential intensity and genesis regions in the North Atlantic during the Last Interglacial. *Geophys. Res. Lett.* **48**, e2021GL093946 (2021).

40. C. S. M. Turney *et al.*, A global mean sea surface temperature dataset for the last interglacial (129–116 ka) and contribution of thermal expansion to sea level change. *Earth Syst. Sci. Data* **12**, 3341–3356 (2020).
41. X. Li *et al.*, A high-resolution climate simulation dataset for the past 540 million years. *Sci. Data* **9**, 371 (2022).
42. K. Emanuel, R. Sundararajan, J. Williams, Hurricanes and global warming: Results from downscaling IPCC AR4 simulations. *Bull. Am. Meteorol. Soc.* **89**, 347–368 (2008).
43. B. Pittet, G. Suan, F. Lenoir, L. V. Duarte, E. Mattioli, Carbon isotope evidence for sedimentary discontinuities in the lower Toarcian of the Lusitanian Basin (Portugal): Sea level change at the onset of the Oceanic Anoxic Event. *Sediment. Geol.* **303**, 1–14 (2014).
44. Y. van Breugel, M. Baas, S. Schouten, E. Mattioli, J. S. Sinninghe Damsté, Isorenieratane record in black shales from the Paris Basin, France: Constraints on recycling of respired CO_2 as a mechanism for negative carbon isotope shifts during the Toarcian oceanic anoxic event. *Paleoceanography* **21**, PA4220 (2006).
45. H. J. Röhl, A. Schimd-Röhl, W. Oschmann, A. Frimmel, L. Schwark, The posidonia shale of SW-germany: An oxygen-depleted ecosystem controlled by sea level and paleoclimate. *Palaeogeogr. Palaeoclimatol. Palaeoecol.* **165**, 27–52 (2001).
46. N. Thibault *et al.*, The wider context of the lower jurassic toarcian oceanic anoxic event in yorkshire coastal outcrops, UK. *P. Geologist. Assoc.* **129**, 372–391 (2018).
47. J. Trabucho-Alexandre, R. Dirkx, H. Veld, G. Klaver, P. L. de Boer, Toarcian black shales in the dutch central graben: Record of energetic, variable depositional conditions during an Oceanic Anoxic Event. *J. Sediment. Res.* **82**, 104–120 (2012).
48. S. P. Hesselbo, H. C. Jenkyns, L. V. Duarte, L. C. Oliveira, Carbon-isotope record of the early Jurassic (Toarcian) Oceanic Anoxic event from fossil wood and marine carbonate (Lusitanian Basin, Portugal). *Earth Planet. Sci. Lett.* **253**, 455–470 (2007).
49. J. W. Hurrell *et al.*, The community earth system model: A framework for collaborative research. *Bull. Am. Meteorol. Soc.* **94**, 1339–1360 (2013).
50. P. Liu *et al.*, Large influence of dust on the precambrian climate. *Nat. Commun.* **11**, 1–8 (2020).
51. X. Li *et al.*, Climate variations in the past 250 million years and contributing factors. *Paleoceanogr. Paleoclimatol.* **38**, e2022PA004503 (2023).
52. M. Zhang, Y. Liu, J. Zhang, Q. Wen, AMOC and climate responses to dust reduction and greening of the Sahara during the mid-Holocene. *J. Clim.* **34**, 4893–4912 (2021).
53. D. J. Lunt *et al.*, DeepMIP: Model intercomparison of early Eocene climatic optimum (EECO) large-scale climate features and comparison with proxy data. *Clim. Past* **17**, 203–227 (2021).
54. A. M. Haywood *et al.*, The pliocene model intercomparison project phase 2: Large-scale climate features and climate sensitivity. *Clim. Past* **16**, 2095–2123 (2020).
55. C. R. Scotese, N. Wright, PALEOMAP paleodigital elevation models (PaleoDEMS) for the Phanerozoic. Earthbyte. https://www.earthbyte.org/paleodem-resource-scotese-and-wright-2018. Deposited 11 August 2018.
56. T. Müller *et al.*, Assessing anoxia, recovery and carbonate production setback in a hemipelagic tethyan basin during the toarcian oceanic anoxic event (Western Carpathians). *Glob. Planet. Change* **195**, 103366 (2020).
57. D. O. Gough, Solar interior structure and luminosity variations. *Sol. Phys.* **74**, 21–34 (1981).
58. D. J. Lunt *et al.*, The DeepMIP contribution to PMIP4: Experimental design for model simulations of the EECO, PETM, and pre-PETM (version 1.0). *Geosci. Model Dev.* **10**, 889–901 (2017).
59. K. A. Emanuel, A statistical analysis of tropical cyclone intensity. *Mon. Weather Rev.* **128**, 1139–1152 (2000).
60. M. Bister, K. A. Emanuel, Low frequency variability of tropical cyclone potential intensity 1. Interannual to interdecadal variability. *J. Geophys. Res. Atmos.* **107**, 4801 (2002).
61. D. M. Gilford, S. Solomon, K. A. Emanuel, On the seasonal cycles of tropical cyclone potential intensity. *J. Clim.* **30**, 6085–6096 (2017).
62. S. Shields, A. A. Wing, D. M. Gilford, A global analysis of interannual variability in potential and actual tropical cyclone intensities. *Geophys. Res. Lett.* **47**, e2020GL089512 (2020).
63. C. L. Bruyère, G. J. Holland, E. Towler, Investigating the use of a genesis potential index for tropical cyclones in the north atlantic basin. *J. Clim.* **25**, 8611–8626 (2012).
64. M. Zhang, L. Zhou, D. Chen, C. Wang, A genesis potential index for estern north pacific tropical cyclones by using oceanic parameters. *J. Geophys. Res. Oceans* **121**, 7176–7191 (2016).
65. K. A. Emanuel, Downscaling CMIP5 climate models shows increased tropical cyclone activity over the 21st century. *Proc. Natl. Acad. Sci. U.S.A.* **110**, 12219–12224 (2013).
66. K. A. Emanuel, Tropical cyclone activity downscaled from NOAA-CIRES reanalysis, 1908–1958. *J. Adv. Model. Earth Syst.* **2**, 1 (2010).
67. R. L. Korty, S. J. Camargo, J. Galewsky, Tropical cyclone genesis factors in simulations of the last glacial maximum. *J. Clim.* **25**, 4348–4365 (2012).
68. F. S. R. Pausata *et al.*, 2017: Tropical cyclone activity enhanced by sahara greening and reduced dust emissions during the african humid period. *Proc. Nat. Acad. Sci. U.S.A.* **114**, 6221–6226 (2017).
69. Q. Yan, R. L. Korty, Z. Zhang, H. Wang, Evolution of tropical cyclone genesis regions during the Cenozoic era. *Nat. Commun.* **10**, 3076 (2019).
70. R. Rousseau-Rizzi, K. Emanuel, Natural and anthropogenic contributions to the hurricane drought of the 1970s–1980s. *Nat. Commun.* **13**, 5074 (2022).
71. P. M. Finocchio, S. J. Majumdar, A statistical perspective on wind profiles and vertical wind shear in tropical cyclone environments of the northern hemisphere. *Mon. Weather Rev.* **145**, 361–378 (2017).
72. Z. Zeng, Y. Wang, L. Chen, A statistical analysis of vertical shear effect on tropical cyclone intensity change in the north atlantic. *Geophys. Res. Lett.* **37**, L02802 (2010).
73. B. Tang, K. Emanuel, A ventilation index for tropical cyclones. *Bull. Am. Meteorol. Soc.* **93**, 1901–1912 (2012).
74. D. S. Nolan, E. D. Rappin, K. A. Emanuel, Tropical cyclogenesis sensitivity to environmental parameters in radiative–convective equilibrium. *Quart. J. Roy. Meteor. Soc.* **133**, 2085–2107 (2007).
75. Q. Yan *et al.*, Modeled tropical cyclone activity and climate during the early Toarcian hyperthermal. *Zenodo*. https://zenodo.org/record/7972338. Deposited 25 May 2023.